COAXIAL INJECTION OF HYDROGEN-NITROGEN AT SUPERCRITICAL CONDITIONS

SPACE PROPULSION 2022
ESTORIL, PORTUGAL | 09 – 13 MAY 2022

Leandro Magalhães [(1)], André Silva [(1)], Jorge Barata [(1)]

[(1)] *AEROG-LAETA, University of Beira interior, Covilhã 6201-001, Portugal, leandro.magalhaes@ubi.pt*

KEYWORDS: coaxial supercritical injection, incompressible variable density approach, Liquid Rocket Engines

ABSTRACT:

Transcritical and supercritical coaxial injection is modelled for a nitrogen-hydrogen coaxial configuration characteristic of the conditions present in liquid rocket engines, with a central high-density low-velocity nitrogen jet and a low-density high-velocity hydrogen jet. Multispecies modelling follows an incompressible variable density approach which demonstrates itself as a valid alternative to the commonly fully compressible formulations encountered in the literature. The results show agreement with the experimental data and compressible formulation in terms of the species radial density profiles maximum values.

1. INTRODUCTION

The mixing efficiency of propellants and oxidizers characteristic of the combustion / thrust chambers of liquid rocket engines constitutes a set of highly coupled and complex physical phenomena. While the overall increase of pressure and temperature leads to an efficiency gain and emission reduction, they also propel the mixtures to exceed their critical point and reach supercritical states. At such conditions, thermodynamic singularities are taken into account in numerical modelling tools by including real gas equations of state and suitable models for describing transport properties into the computational algorithms. Over the past 20 years, the interest in modelling and understanding such phenomena increased. However, potential developments are hindered due to the lack of experimental data for models' validation. Heavily relying on shadowgraphy [10] and Raman scattering [15] techniques, the available experimental data allowed for the description of the supercritical state as a single-phase occurrence, resembling a gas jet-like behaviour.

Multispecies coaxial injection [4] is a more difficult phenomena to model than single-species injection [6], yet it's crucial in liquid rocket engine (LRE) design. The critical characteristics of the mixture, for example, are not fixed values and are susceptible to local dynamical change [5]. These must be considered while creating mixing rules. A consequence of the dynamical shifting nature of the critical point in multicomponent mixing relates to the fact that conditions may exist in the chamber below those of the individual species' critical point [9], as for instance the temperature, in which case transcritical behaviour will influence the jet behaviour and increase the complexity of the phenomena taking place. The dynamical shift of the critical point in multicomponent mixtures explain why surface tension was reported at pressures above the critical point value [10].

Several developments into the description of transcritical mixing have taken place in recent years. [7] extended the incompressible but variable density hypothesis [1] into the description of transcritical nitrogen, showing good agreement with experimental data in the prediction of jet spreading rates and axial density profiles, while [8] developed an analytical framework for the prediction of the conditions in which phase equilibrium occurs in multicomponent mixing. Further studies on coaxial injection [11,14] were performed detailing the interactions between a central high-density low-velocity stream and a coaxial low-density high-velocity one, following the behaviour taking place in LRE's injection systems.

Temporal mixing layers [12] have traditionally been the go to configuration to study multicomponent mixing, such as nitrogen-heptane [13].

In the present work, we employ an incompressible variable density hypothesis [1] for the study of coaxial supercritical hydrogen-nitrogen injection into a chamber filled with nitrogen at supercritical conditions [2]. By including both injectors in the computations, we are able to assess the thermal effects [3] and how they influence jet mixing and development.

The rest of this manuscript is structured as follows. First, the test circumstances for which experimental data are available are provided, then the mathematical/physical models that form the foundation of the RANS technique are analysed

and discussed in order to determine their performance, benefits and limitations, and function in the whole process. The influence of temperature on the processes related to transcritical and supercritical injection are analyzed in the results section. Finally, the conclusions highlight the key results.

2. EXPERIMENTAL CONDITIONS REVIEW

The experimental results are consistent with the work of [2], obtained with the Raman scattering technique. Nitrogen is fed through the central post at either supercritical (D4) or transcritical conditions, as specified in Tab. 1. (E4).

The injectors are 90 mm long, with a diameter of 1.9 mm for the central injector and 2.4 mm for the coaxial injector. The combustion chamber, on the other hand, is 500 mm long and 100 mm in diameter.

The injectors and chamber have isothermal walls, but the faceplate has an adiabatic wall boundary condition [6].

Table 1. Experimental conditions [2].

Case	$v_{N2,jet}$ [m/s]	$V_{H2,jet}$ [m/s]	$T_{N2,jet}$ [K]	$T_{H2,jet}$ [K]	$\rho_{N2,jet}/\rho_{H2,jet}$	$v_{N2,jet}/v_{H2,jet}$
D4	5.0	60	140	270	43.1	0.083
E4	5.0	120	118	270	166	0.042

3. MATHEMATICAL MODELLING
3.1. Governing Equations and Turbulence Modelling

The governing equations are written for a multispecies mixture with no reaction. As such, the system of partial differential equations comprises a mass conservation equation for each of the individual species and one conservation equation for momentum and energy. In this way, turbulent mixing will drive jet development and the mixing layer formation, where each cell-volume will have volume fraction of both species. Eqs. 1 to 3 represent the Favre-averaged conservation of mass, momentum and energy, respectively, where ρ is the density, u the velocity vector, x the length vector, i and j the directional vectors, p the pressure, τ the stress tensor, q the heat flux and H the total enthalpy.

$$\frac{\partial \bar{\rho}\widetilde{u_i}}{\partial x_i} = 0 \qquad \text{Eq.1}$$

$$\frac{\partial}{\partial x_j}\left(\bar{\rho}\widetilde{u_i}\widetilde{u_j}\right) = -\frac{\partial \bar{p}}{\partial x_i} + \frac{\partial \overline{\tau_{ij}}}{\partial x_j} - \frac{\partial \bar{\rho}\widetilde{u_i''u_j''}}{\partial x_j} \qquad \text{Eq.2}$$

$$\frac{\partial \bar{\rho}\widetilde{u_j}\widetilde{H}}{\partial x_j} = \frac{\partial \overline{\tau_{ij}u_i}}{\partial x_j} - \frac{\partial \widetilde{u_i}\bar{\rho}\widetilde{u_i''u_j''}}{\partial x_j} - \frac{\partial}{\partial x_j}\left(\bar{q_j} + \bar{\rho}\widetilde{u_j''h''}\right) \qquad \text{Eq.3}$$

The resultant Reynolds stress tensor is approximated by the Boussinesq hypothesis of Eq. 4, where κ is the turbulence kinetic energy, μ_t is the eddy viscosity, and δ_{ij} is Kronecker's delta function.

$$-\bar{\rho}\widetilde{u_i''u_j''} = -\frac{2}{3}\rho\kappa\delta_{ij} + \mu_t\left(\frac{\partial \widetilde{u_i}}{\partial x_j} + \frac{\partial \widetilde{u_j}}{\partial x_i} - \frac{2}{3}\frac{\partial \widetilde{u_k}}{\partial x_k}\delta_{ij}\right) \qquad \text{Eq.4}$$

The turbulent heat flux, $\bar{\rho}\widetilde{u_j''h''}$, is modeled using Eq. 5, where Pr_t is the turbulent Prandtl number representing the ratio of momentum eddy diffusivity to heat eddy diffusivity and T the temperature.

$$\bar{\rho}\widetilde{u_j''h''} = -\frac{c_p}{Pr_t}\frac{\partial \widetilde{T}}{\partial x_j} = -\frac{\mu_t}{Pr_t}\frac{\partial \widetilde{h}}{\partial x_j} \qquad \text{Eq.5}$$

The system is closed by the standard κ-ε turbulence model of [17], where the velocity and length scales are determined from field equations.

3.2. Equation of State

In the present work the Peng-Robinson equation of state [18], where R is the gas constant, v_m the molar volume, while a and b represent intermolecular effects.

$$p = \frac{RT}{v_m-b} - \frac{a(T)}{v_m(v_m+b)+b(v_m-b)} \qquad \text{Eq.6}$$

3.3. Transport Properties

Thermal conductivity and dynamic viscosity analyses take into consideration the specific behaviour of these variables at the critical point [19].

Dynamic viscosity, μ, is calculated using Eq.7, as a contribution of low-pressure viscosity, μ_k, and a high-pressure correction component, μ_p. Additional parameters are specified in Eqs. 7 to 18, where μ_0 is the dilute gas viscosity, G_1, G_2, and y are auxiliary parameters, and A_i linear interpolations of the acentric factor, reduced dipole moment, and association factor. M is the molar mass, T is the dimensionless temperature, v_c is the critical volume, F_c is a parameter accounting for molecular structure and polar effects, μ_r is the dimensionless dipole moment, κ a correction factor for hydrogen-bonding effects and Boltzmann's constant in the dimensionless temperature definition, ε a potential energy parameter and Ω^* a collision integral whose constants A through H are given by [19].

$$\mu = \mu_k + \mu_p \qquad \text{Eq.7}$$

$$\mu_k = \mu_0\left(\frac{1}{G_2} + A_6 y\right) \qquad \text{Eq.8}$$

$$\mu_p = \left[36.3446^{-6}\frac{(MT_c)^{0.5}}{v_c^{2/3}}\right] A_7 y^2 G_2 \exp\left(A_8 + \frac{A_9}{T^*} + \frac{A_{10}}{T^{2*}}\right) \quad \text{Eq.9}$$

$$y = \frac{\rho v_c}{6} \qquad \text{Eq.10}$$

$$G_1 \frac{1-0.5y}{(1-y)^3} \qquad \text{Eq.11}$$

$$G_2 = \left[\frac{A_1(-\exp[-A_4 y])}{y} + A_2 G_1 \exp(A_5 y) + A_3 G_1\right] / (A_1 A_4 + A_2 + A_3) \qquad \text{Eq.12}$$

$$A_i = a_0(i) + a_1(i)\omega + a_2(i)\mu_r^4 + a_3(i)\kappa \quad i = 1,10 \quad \text{Eq.13}$$

$$\mu_r \frac{131\mu}{(v_c T_c)^{1/2}} \qquad \text{Eq.14}$$

$$\Omega^* = \frac{A}{T^{*B}} + \frac{C}{\exp(DT^*)} + \frac{E}{\exp(FT^*)} + GT^{*B}\sin(ST^{*W} - H) \qquad \text{Eq.15}$$

$$F_c = 1 - 0.2756\omega + 0.059035\mu_r^4 + \kappa \quad \text{Eq.16}$$

$$T^* = \frac{\kappa T}{\varepsilon} \qquad \text{Eq.17}$$

$$\mu_r = \frac{131.3\mu}{(v_c T_c)^{0.5}} \qquad \text{Eq.18}$$

Thermal conductivity is evaluated in the same way as dynamic viscosity as reproduced in Eq. 19. The remaining parameters appearing in Eqs. 20 to 29 are the dilute gas thermal conductivity, λ_0, an empirical parameter, β, the thermal capacity at constant volume, c_v and the dependent parameters ψ, α and Z.

$$\lambda = \lambda_k + \lambda_p \qquad \text{Eq.19}$$

$$\lambda_0 \frac{7.452\mu_0 \psi}{M} \qquad \text{Eq.20}$$

$$\mu_0 = 26.69^{-6}\frac{(MT)^{1/2}}{\sigma^2 \Omega^*} \qquad \text{Eq.21}$$

$$\psi = 1 + \alpha\left[\frac{0.215 + 0.28288\alpha - 1.061\beta + 0.26665Z}{0.6366 + \beta Z + 1.061\alpha\beta}\right] \quad \text{Eq.22}$$

$$\alpha = \frac{c_v}{R} - \frac{3}{2} \qquad \text{Eq.23}$$

$$\beta = 0.7862 - 0.7109\omega + 1.3168\omega^2 \quad \text{Eq.24}$$

$$Z = 2 + 10.5T_r^2 \qquad \text{Eq.25}$$

$$\lambda_\kappa = \lambda_0\left(\frac{1}{H_2} + B_6 y\right) \qquad \text{Eq.26}$$

$$\lambda_p = \left[3.0396^{-4}\left(\frac{T_c}{M}\right)^{0.5}\frac{1}{v_c^{2/3}}\right] B_7 y^2 H_2 T_r^{1/2} \quad \text{Eq.27}$$

$$H_2 = \left[\frac{B_1(1-\exp(-B_4 y))}{y} + B_2 G_1 \exp(B_5 y + B_3 G_1)\right] / (B_1 B_4 + B_2 + B_3) \qquad \text{Eq.28}$$

$$B_i = b_0(i) + b_1(i) + b_2(i)\mu_r^4 + b_3(i)\kappa \quad \text{Eq.29}$$

4. NUMERICAL ALGORITHM

To store scalar values at cell centers, the finite volume approach is utilized. The governing equations' diffusive terms are discretized using a second-order central scheme, whereas advective terms are discretized using the QUICK method [20]. The incorporation of first-order upwinding reduces the appearance of non-physical spurious pressure oscillations. This is especially true when a second-order central scheme is used to describe advective fluxes with a grid Péclet number larger than two, indicating that advection has twice the magnitude of diffusion. The QUICK scheme combines high-order accuracy with upwind scheme direction behavior, offering extra stability for advective terms at coarser meshes.

Due to momentum divergence and the insertion of $\frac{\partial \bar{\rho}\widetilde{u_i}}{\partial x_J} = 0$, a pressure-based method is devised in which conservation of mass is implicitly realized by a pressure-based continuity equation. The reasoning behind this approach is given in [21]. The velocity and pressure fields are then computed concurrently, followed by energy conservation and the transfer of turbulence variables until convergence is achieved.

5. RESULTS

Fig. 1 depicts a preliminary result, where we can observe radial profiles of nitrogen. While the mixing layer configuration was chosen so that no interplay of combustion is considered in the study, the experimental data allows to gain insight into the flow behavior in liquid rocket engines. A low-velocity high density nitrogen jet is considered in the inner injector, while the annular jet has a much higher velocity and lower density. The initial region downstream of the injector is governed by the mixing layer growth between the two fluids, which given the high velocity ratio between both streams, results in the entrainment of the central nitrogen, in the sense of a mass transfer process across the interface from the inner potential core into the mixing layer.

The maximum of nitrogen's radial density profiles for case D4 from Tab. 1 is depicted in Fig. 1. On the horizontal axis, the centerline axial distance from the injector exit plane, *x*, is normalized by the injector diameter (*d*), and grid independence was achieved for a typical mesh of 7.9 x10^5 points, as shown in the figure. The experimental data from [2] is compared to the findings of our numerical simulations using an incompressible but variable density formulation, where an initial over-prediction is observed in the maximum of the radial density profiles up to a distance of 7 injector diameters.

The impact of the non-uniform density profile at the

injector's exit, which grows steeper owing to entrainment into the jet of low-density nitrogen in the chamber and the action of heat transfer from the secondary hydrogen stream, causes an initial deterioration over a distance of 6 injector diameters. In this scenario, the injection temperature $T_{N2,jet}$ = 140 K is higher than nitrogen's pseudo-boiling temperature, suggesting a shorter decay than, for example, an injection temperature lower than nitrogen's pseudo-boiling temperature (for example case E4). Despite an initial overestimation of nitrogen density, the qualitative behavior of the trials is consistent with our numerical expectations. In the picture, the large eddy simulation (LES) results of [16], using a compressible formulation, are also shown for comparison. Because the authors did not account for heat transport in the injectors, a tiny potential core is detected up to a distance of around two injector diameters, which differs significantly from the experimental data points. As a result, [16] changed the inflow temperature to match the density found in the potential core and ran another simulation with an injection temperature of $T_{N2,jet}$ = 158.8 K, while retaining the same flow rate and so increasing the injection velocity. This was caused by a constant-valued plug flow profile placed at the chamber entry, as well as a radial profile. In our situation, because we are considering both injectors, we ran an extra simulation with the injection temperature, $T_{N2,jet}$ = 158.8 K, identical to [16], but with the same injection velocity.

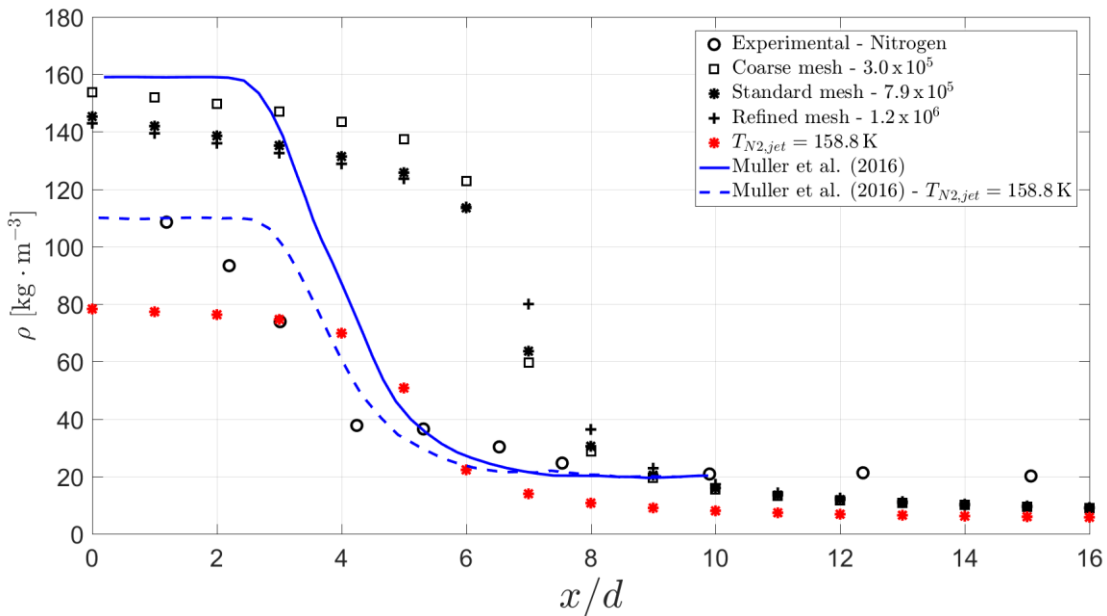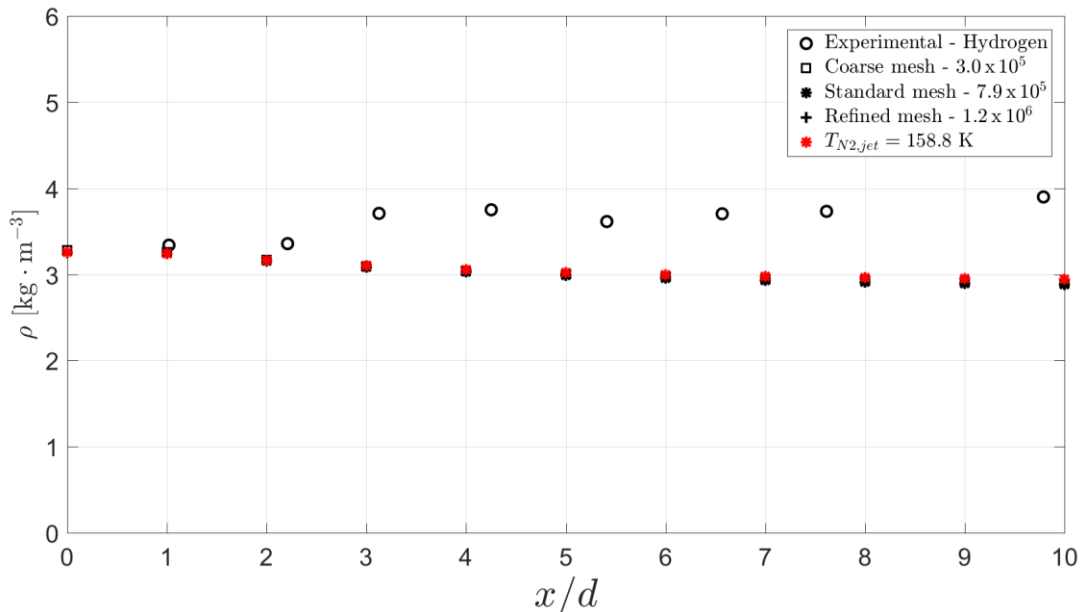Figure 1. Maximum of nitrogen's radial profiles corresponding to case D4.

Figure 2. Maximum of hydrogen's radial profiles corresponding to case D4.

4

Fig. 2 depicts the comparable evolution in the maximum of the radial hydrogen profiles of hydrogen. Following the injection into the chamber, we can see a rise in the density of hydrogen, which [4] attributes to heat transfer from the hydrogen to the nitrogen stream. Our results, on the other hand, show a distinct pattern, with a small density decrease that stays unchanged even for the fitted injection condition of $T_{N2,jet}$ = 158.8 K.

The injection occurs ($T_{N2,jet}$ = 118 K) below the critical temperature of nitrogen ($T_{N2,c}$ = 126.2 K) in scenario E4, as shown in Fig. 3. Similar to instance D4, there is an over-prediction in terms of density values. Our findings show that the nitrogen's density maximum decay rate is the slowest in the first four injector diameters, after which the decay

rate becomes steeper owing to entrainment from the hydrogen stream and chamber nitrogen into the jet. Furthermore, [16] estimate a potential core with a length of two injector diameters and a density far higher than that found experimentally.

As a consequence, a fitting temperature ($T_{N2,jet}$ = 128.8 K) is provided, yielding comparable findings between the compressible formulation of [16] and our incompressible but variable density method. In terms of hydrogen density evolution, Fig. 4 shows a different pattern than in example D4. In this case, hydrogen density is particularly sensitive to changes in nitrogen injection temperature. The heat transfer from the hydrogen into the nitrogen causes the first increase in hydrogen density.
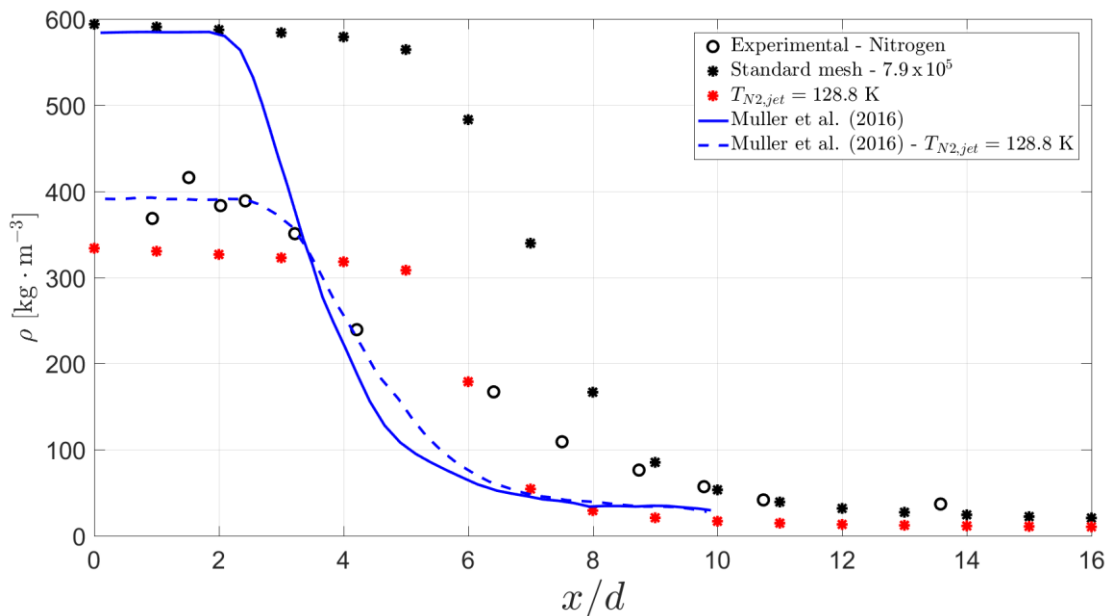

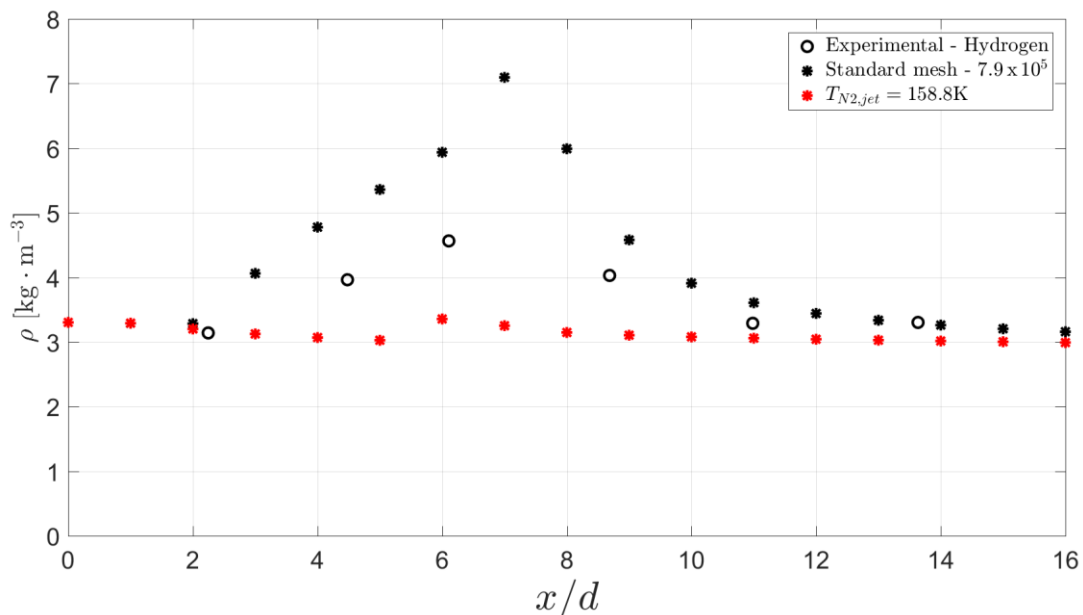Figure 3. Maximum of nitrogen's radial profiles corresponding to case E4.

Figure 4. Maximum of hydrogen's radial profiles corresponding to case E4.

5

6. CONCLUSIONS

In the manuscript we propose to study the coaxial injection of hydrogen and nitrogen stream at supercritical conditions, with velocity and density conditions characteristic and relevant for liquid rocket propulsion, by considering the heat transfer in both injectors. This is intended to serve as a stepping stone for futures studies, dealing with coaxial combustion interplay.

An incompressible variable density formulation is employed to describe the multi-species mixing between the high-density low-velocity central nitrogen and the low-density high-velocity hydrogen. Through comparison with experimental data and with a compressible formulation available from the literature agreement was found for the transcritical and supercritical injection configurations considered. Further studies in the future will focus in the coupling of two-phase flow modelling with the proposed methodology.

7. ACKNOWLEDGMENTS

8. REFERENCES

1. Barata, J., Gökalp, I. & Silva, A. (2003). Numerical Study of Cryogenic Jets under Supercritical Conditions. *J. Propuls. Power* **19**(1), 142-147.

2. Oschwald, A., Schik, M., Klar, M. & Mayer, W. (1999). Investigation of Coaxial LN2/GH2 Injection at Supercritical Pressure by Spontaneous Raman Scattering. *In 35th Joint Propulsion Conference and Exhibit*, AIAA paper 992887.

3. Banuti, D.T & Hannemann, K. (2016). The Absence of a Dense Potential Core in Supercritical Injection: A Thermal Break-up Mechanism. *Phys. Fluids* **28**(3), 035103.

4. Immich, H. & Mayer, W. (1997). Cryogenic Liquid Rocket Engine Technology Developments within the German National Technology Programme. *In 33rd Joint Propulsion Conference and Exhibit*, AIAA paper 1997-2822.

5. Polikhov, S.A. & Segal, C. (2007). Experimental Study of Subcritical to Supercritical Jet Mixing. *In 45th AIAA Aerospace Sciences Meeting and Exhibit*, AIAA paper 2007-569.

6. Magalhães, L.B., Silva, A.R.R. & Barata, J.M.M. (2022). Contribution to the Physical Description of Supercritical Cold Flow Injection: The Case of Nitrogen. *Acta Astronautica* **190**(2022). 251-260.

7. Magalhães, L., Cleto, J., Silva, A. & Barata, J. (2022). Description of an Incompressible Variable Density Approach for the Modeling of Supercritical Fluid Flows. *8th Edition of the Space Propulsion Conference*, **5**(2022).

8. Tudisco, P. & Menon, S. (2020). Analytical Framework for Real-gas Mixtures with Phase-equilibrium Thermodynamics. *J. Supercrit. Fluids* **164**(2020), 104929.

9. Traxinger, C., Zips, J. & Pfitzner, M. (2019). Single-phase Instability in Non-premixed Flames under Liquid Rocket Engine Relevant Conditions. *J. Propuls. Power* **35**(4), 1-15.

10. Mayer, W., Ivancic, B., Schik, A., & Hornung, U. (1998). Propellant Atomization in LOX/GH2 Rocket Engines. *In 34th AIAA/ASME/SAE/ASEE Joint Propulsion Conference and Exhibit*, AIAA paper 98-3685.

11. Jarrahbashi, D., Sirignano, W.A., Popov, P.P. & Hussein, F. (2016). Early Spray Development at High Gas Density: Hole, Ligament and Bridge Formations. *J. Fluid Mech.* **792**(2016), 186-231.

12. Miller, R., Harstad, K. & Bellan, J. (2001). Direct Numerical Simulations of Supercritical Fluid Mixing Layers Applied to Heptane-nitrogen. *J. Fluid Mech.* **436**(2001), 1-39.

13. Okong'o, N.A. & Bellan, J. (2002). Direct Numerical Simulation of a Transitional Supercritical Binary Mixing Layer: Heptane and Nitrogen. *J. Fluid Mech.* **464**(2002), 1-34.

14. Favre-Marinet, M., Camano, E.B. and Sarboch, J. (1999). Nearfield of Coaxial Jets with Large Density Differences. *Exp. Fluids* **26**(1999), 97-106.

15. Mayer, W., Teelar, J., Branam, R., Schneider, G. & Hussong, J. (2003). Raman Measurements of Cryogenic Injection at Supercritical Pressure. *Heat and Mass Transfer* **39**(2003), 709-719.

16. Müller, H., Pfitzner, M., Matheis, J., & Hickel, S. (2016). Large-Eddy Simulation of Coaxial LN2/GH2 Injection at Trans- and Supercritical Conditions. *J. Propuls. Power* **32**(2), 46-56.

17. Launder, B.E. & Spalding, D.B. (1972). Lectures in Mathematical Models of Turbulence. *Academic Press*, London, UK.

18. Peng, D. & Robinson, D.B. (1976). A New Two-constant Equation of State. *Ind. Eng. Chem.* **15**(1), 59-64.

19. Chung, T.H., Ajlan, M., Lee, L.L. & Starling, K. (1988). Generalized Multiparameter Correlation for Nonpolar and Polar Fluid Transport Properties. *Ind. Eng. Chem Res.* **27**(4), 671-679.

20. Leonard, B.P. (1979). A Stable and Accurate Convective Modelling Procedure based on Quadratic Upstream Interpolation. *Comput. Methods Appl. Mech. Eng.* **19**(1), 59-98.

21. Jarczyk, M. & Pfitzner, M. (2012). Large Eddy Simulation of Supercritical Nitrogen Jets. *In 50th AIAA Aerospace Sciences Meeting including the New Horizons Forum and Aerospace Exposition.* AIAA paper 2012-1270